RSC Advances

PAPER

View Article Online
View Journal | View Issue

Cite this: *RSC Adv.*, 2016, **6**, 15577

Charges on nano-islands and fibrils of poly(3-hexylthiophene-2,5-diyl) – light-modulation, injection and transportation†

Haixia Xuan, Xi Chen, Yinghui Wu, Kena Song, Yuenan Li and Ruchuan Liu*

Received 25th December 2015
Accepted 27th January 2016

DOI: 10.1039/c5ra27711f

www.rsc.org/advances

The impact of the nanostructures of conjugated polymers on their electronic properties is significant. We notice that poly(3-hexylthiophene-2,5-diyl) (P3HT) can form nano-islands and nano-fibrils, and both of them show an similar single-layer thickness (~1.5–1.6 nm) as evaluated by atomic force microscopy (AFM). The Raman spectra indicate the highest degree of chain planarity and crystallinity in the nano-islands. By using scanning Kelvin probe microscopy (SKPM) and electrostatic force microscopy (EFM), we image the surface potential at the nanometer scale and quantitatively estimate the charges on these nanostructures as modulated by light. Both results are consistent with each other: the surface potential increases on switching on the light, and the photo-induced charges are around 15–25% and positive. A similar amount of the photo-induced charges in both P3HT islands and fibril is consistent with the π–π stacking nature of these nanostructures. As P3HT is a hole-conducting molecule, positive charges are found easily injected into a single island by a positively biased EFM tip, and then the injected charges are able to propagate all over the island.

1. Introduction

π-Conjugated materials have been the focus of recent research due to their potential application in cost-efficient, solution-processable, and flexible electronic and optoelectronic devices, such as field effect transistors and solar cells.[1–4] As a conjugated polymer, poly(3-hexylthiophene-2,5-diyl) (P3HT), which consists of a rather rigid backbone with pendant alkyl side chains, is an interesting conjugated system characterized by hierarchical order at three main length scales, and has gained increasing interest as active layers in numerous organic electronic devices.[5–7] The structure of P3HT, the intrinsic crystallization mode, and the behaviors of this class of conjugated polymers have been extensively studied.[7–9] X-ray diffraction (XRD) analysis[10,11] and grazing-incidence X-ray diffraction have been used to analyze the P3HT crystal structure and then to identify the edge-on side chains and desirable parallel orientation of π–π stacking planes of P3HT with respect to solid substrates.[12–20] Recently, free-standing P3HT thin films consisting of H- (side-by-side orientations) and J-aggregated (head-to-tail orientations) nanowires were prepared by the vacuum filtration method separately, and a shorter interchain stacking distance was found in J-aggregates than in H-aggregates.[21,22] In the model developed by Spano, H- and J-aggregation can be identified based on the absorption intensity ratio of A_{0-0}/A_{0-1}.[23,24] J-Aggregates exhibits a ratio of A_{0-0}/A_{0-1} slightly larger than 1, while the ratio for traditional H-aggregates is typically between 0.5–0.8. UV-Vis absorption, fluorescence emission, and Raman spectra have been used to characterize the polymer and demonstrated that P3HT chains possess long-range intrachain order (planarity) that suppressed interchain exciton coupling, and π–π stacked P3HT chains can show behaviors of both H- and J-aggregates. This opens up new possibilities for controlling electronic coupling through noncovalent stacking interactions.[18]

Synthesis and characterization of one-dimensional (1D) nanofibers based on P3HT have been reported.[25] Their unique properties, such as high aspect ratios and chemical and mechanical stability, made them candidates for high performance components for future organic devices.[26–28] Ren *et al.* used nanowires of P3HT combined with quantum dots to change the power conversion efficiency of the photovoltaic application[29] and Guo *et al.* investigated the electrochemical properties of polymer with quantum dots.[30] In addition, the electrical properties of nanostructures are essential for their applications as electrical switching and electrochromic devices,[31] while the magnetoresistance effect has also been found in other organic/carbon-based nanocomposites.[32,33] Nevertheless, the understanding of the nanostructure of the fibrils and their charge capability as well as the light modulation of charges inside is still in urgent need.

Department of Physics, Chongqing University, Chongqing 401331, P. R. China. E-mail: phyliurc@cqu.edu.cn

† Electronic supplementary information (ESI) available: Description of the quantification of photo-induced charges for samples. See DOI: 10.1039/c5ra27711f

In this article, we studied the optical and electrical properties of P3HT-based nano-structures. In the self-assembled fibrils of P3HT and the nano particle-assisted assembly of P3HT nano-islands, the characteristic single-layer thickness were revealed by atomic force microscopy (AFM), and the molecular arrangement of these nanostructures was then studied by Raman spectra in a similar way as reported.[34,35] As expected to vary among these nano structures, their optoelectronic and charge transportation property were investigated by scanning Kelvin probe microscopy (SKPM) and electrostatic force microscopy (EFM). While the layered structure was found in the nano-islands of P3HT, the EFM results indicated that both the nano-islands and fibrils of P3HT were capable to store charges. However, only the crystalline islands were found to be able to delocalize injected holes among their layers, indicating the better intermolecular π–π stacking. The results provide detail information of the charges distribution of various P3HT nano-structures while switching light on/off, which is important for the solar cell application, and then the results demonstrate a new approach in studying solar cell materials.

2. Experimental methods

P3HT islands preparation

Before experiment indium-tin oxide (ITO) (8 Ω sq.$^{-1}$), glass slide and silicon wafer (Si/SiO_2) were cleaned by deionized water, acetone and ethanol absolute for 20 min each. After cleaning, all substrates were rinsed by deionized water and dried with clean air. Poly(3-hexylthiophene-2,5-diyl) (P3HT) (PDI ≤ 2, M_w = (15 000–45 000) g mol^{-1}, Sigma Aldrich Chemical Co.) was dissolved in chlorobenzene (Aladdin Inc.) with stirring (7 mg ml^{-1}) for an hour at 90 °C, then the solution was cooled to room temperature by water bath, the prepared solution was then kept in dark. CdS/CdSe powders (Aladdin Inc.) were further grinded by a Fritsch planetary ball milling machine (Pulverisette 7) with agate balls, at 200 rpm for 2 hours. The grinded nanoparticles were suspended in chlorobenzene at a concentration of 30 mg ml^{-1}, then centrifuged 3000 rpm for 20 s, and the supernatant was mixed with the P3HT solution at a volume ratio of 1 : 1. The mixed solutions were spin coated onto ITO and Si/SiO_2 substrates at a speed of 2000 rpm to form nano-islands.

P3HT nanofibrils preparation

Nano fibrils of P3HT were prepared similar as reported.[36] The P3HT solution in chlorobenzene (7 mg ml^{-1}) at 90 °C was cooled to room temperature at a rate of 10 °C h^{-1} in a water bath, and then mixed with ethanol (99.8%) at a 95 : 5 volume ratio for 30 min before spin-coating. Finally, the solution was spin coated onto cleaned glass slides at a speed of 3000 rpm to form nano-fibrils.

UV-Vis and Raman characterization

A UV-3600 spectrophotometer (Shimadzu, Japan) was used for the absorption spectra in the range of 380–760 nm. Raman spectra were recorded by a commercial Micro Raman spectrometer (Horiba), using an excitation laser beam with a wavelength of 532 nm (~0.05 mW) and a beam diameter of ~2 μm, and an acquisition time of 30 s.

AFM, SKPM and EFM

Both SKPM and EFM were implemented on an AFM platform (MFP-3D, Asylum Research). SKPM was used to determine the difference in the surface potential between the conducting probe (Multi75E-G, Budget sensor) and the sample. The Pt/Cr coated silicon tip had an oscillation frequency $f_0 \approx 60$ kHz, spring constant of 1–5 N m^{-1} (usually ~2.8 N m^{-1}), and a quality factor Q of ~186. SKPM measurements were carried out in the two-pass manner. The first pass was used to determine the topography of the surface, and was done exactly like a standard AC mode scan line in AFM. The second pass was done by retracing the topography plus an additional z distance of 50 nm, while an AC voltage at a frequency of 60–65 kHz and a tunable DC voltage were applied between the tip and the substrate. The DC voltage was adjusted at each point to cancel the force at the AC frequency, and accordingly the value was recorded as the potential difference.

EFM measurements were also conducted in a similar two-pass manner, but different from SKPM only in the second pass. During the second pass, the tip was maintained in the electrostatic force region, oscillated at its resonance frequency, and biased by applying a DC voltage (V_{EFM}) without the AC voltage as in SKPM. The electric field created a force gradient between the tip and the sample that caused a shift in the resonance frequency of the cantilever. The shift in resonance in turn caused a shift in the phase lag between the drive and response of the cantilever. Finally, the phase shift due to the electrostatic force at different voltage was measured.

The whole AFM system is integrated on top of an optical microscope (IX71, Olympus), so the sample can be easily illuminated through a 40× objective in the measurements. A sapphire laser (Coherent, SAPPHIRE 488-120 FP) with a wavelength of 488 nm was used for light excitation, and laser intensity on the samples is ~0.2 W cm^{-2}.

All the experiments were conducted in similar conditions such as ambient environment and room temperature.

3. Results and discussion

The similarity and dissimilarity between P3HT nano-islands and fibrils

Fig. 1 shows the characterizations of P3HT spin-coating samples, and the nano-fibrils, films and islands, can be clearly identified from the AFM images (Fig. 1a–d). While simply spin-coating of P3HT solution results in a flat film as shown Fig. 1b, using the same protocol as Sun *et al.* reported,[36] the spin-coated P3HT can self-assemble into nano fibrils as shown in Fig. 1a. Though the heights of the fibrils are not very uniform, they are more or less around 1.6 nm as indicated by a line scan across fibrils (blue line in Fig. 1a). More specific, statistical analysis of fibrils gives a value of 1.6 ± 0.1 nm in height (insert of Fig. 1a). It has been shown that in the well π–π stacking

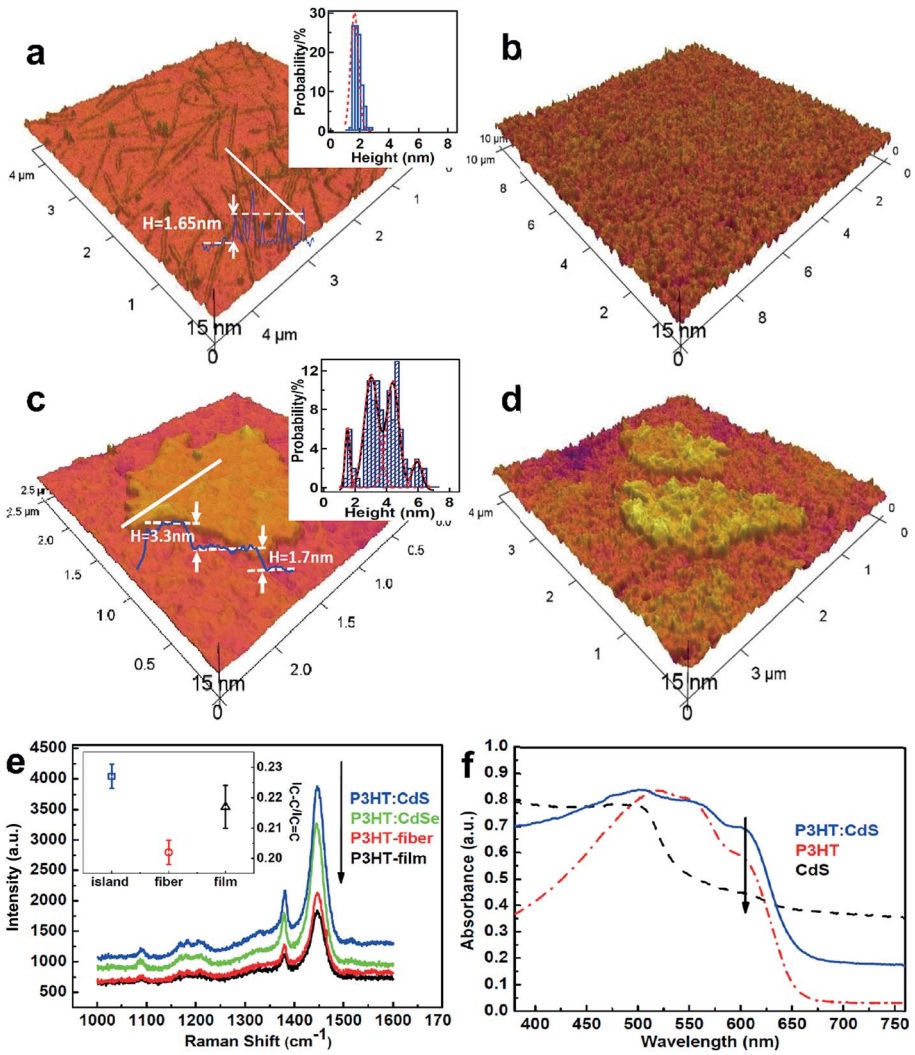

Fig. 1 Topography, Raman spectra and UV-visible absorption spectra of the P3HT islands and P3HT nano-fibrils: (a) the topography of P3HT nano-fibrils and the histogram of the height (insert), with an average of 1.6 ± 0.1 nm; (b) the topography of a pure P3HT film without nano-island or nano-fibrils, with the RMS of 1.2 nm; and the topography of P3HT films shows nano-islands when mixed with (c) CdS and (d) CdSe nano-particles, respectively. The insert in (c) is the histogram of the height of all the nano-islands, and it is clearly that there are 4 Gauss peaks and the peak heights are 1.5 ± 0.1 nm, 3.0 ± 0.1 nm, 4.4 ± 0.1 nm, 5.9 ± 0.2 nm, respectively; (e) Raman spectra of different P3HT nanostructures and illustration of C–C/C=C intensity ratios; (f) UV-Vis absorption spectra of thin films of CdS, pure P3HT, and P3HT:CdS.

of P3HT crystal-like structures, the crystal plane spacing of ~1.6 nm in the direction of the side chains and the inter-chain π–π stacking distance of ~0.38 nm are expected[13,19,37] and both numbers are also the size of single molecules. Thus, gradually cooling of the well dissolved P3HT to room temperature helps the self-assembly of P3HT fibrils, which are likely in an ordered molecular arrangement. In addition, a dramatic color change from bright orange to dark browning-purple is found during the cooling of the P3HT solution[38] before spin-coating also implies inter-chain π–π coupling, which changes the absorption of molecules.

P3HT nano-islands (Fig. 1c and d) were formed by spin-coating the mixed solution of P3HT with CdS or CdSe nano-particles. The size of CdS nanoparticles is ~1.5 ± 0.1 nm (ESI Fig. S1†), so most nanoparticles are buried in the polymer films and absent in the AFM images. These islands are layered structures. In Fig. 1c, two layers can be seen and the line profile (blue line) show two staircases, one at a height of ~1.7 nm and the other ~3.3 nm. The histogram of the heights of all islands shows four peaks, and can be well fitted by four Gaussian peaks at 1.5 ± 0.1 nm, 3.0 ± 0.1 nm, 4.4 ± 0.1 nm, and 5.9 ± 0.2 nm, respectively. These peak values are all the multiples of ~1.5 nm, which is very close to the height of the fibrils found in Fig. 1a. This indicates that in the islands, each layer is likely a molecular layer of π–π stacking P3HT. Here, the nanoparticles play a positive role in formation of these P3HT nano-islands, as indicated by some of these islands are coupled with CdS/CdSe nanoparticles (ESI Fig. S2†).

In order to verify their molecular architectures, Raman scattering has been used, because π–π stacking of P3HT chains may change the vibrations in the conjugated system as a results of the coupling. Fig. 1e shows the Raman spectra of

corresponding samples. The two major Raman peaks around 1380 and 1450 cm^{-1} are usually described as intra-ring C–C and C=C symmetric backbone stretches, respectively. The C–C/C=C intensity ratio is sensitive to the degree of chain planarity and conjugation lengths of P3HT crystallinity.[34,39] Our Raman results (Fig. 1e) show that the ratios of I_{C-C} to $I_{C=C}$ are 0.227 ± 0.004, 0.200 ± 0.008, and 0.217 ± 0.007 for nano-island, fibrils and no feature film, respectively. The higher ratio for nano-island indicates the well parallel ordered π–π stacking of P3HT molecules, as suggested by Gao *et al.*[34] However, though AFM morphology shows similar height of fibrils and one layer of the islands, the ratio in Raman spectra for fibrils is smaller than for normal films. This indicates a different way of molecular stacking, *e.g.* instead of parallel, twisting of the π units along the fibrils.

Surface potential of the nanostructures in response to laser excitation

The previous studies on the P3HT-*b*-P3MT nanofibers revealed that HOMO energy of aggregates could be further tuned by varying polymer chain order in formed nanostructures.[40,41] The structural analysis of the nano-islands and fibrils by AFM imaging and Raman spectra indicates various molecular arrangements in these nano structures, so the variations in their electronic energy levels are expected. As a powerful derivative of AFM, SKPM is capable of to measure the surface potential (SP) of samples at the nanometer scale, which is closely related to the charge distribution.[42] Especially, it can quantitatively evaluate the potential difference between samples and substrates. Fig. 2 shows the typical morphology and SP images of P3HT nano-islands and fibrils, along with the histograms of surface potential as modulated by the excitation light (488 nm laser line), and more SP images can be found in ESI.† In these SKPM images, higher (positive) SP values are observed for nano-islands than the surrounding substrates, while the relative SP of fibrils is only a couple of millivolts higher. The positive SP values is consistent with the p-type nature of P3HT as an organic semiconductor. Taking the substrates as the reference, we can quantitatively compare the relative SP between P3HT samples, and their changes upon light excitation as well. For nano-islands, the relative SP changes from 24.3 ± 7.1 mV in dark to 28.8 ± 8.6 mV under illumination (Fig. 2d), while for fibrils, the increment in the value is even less, from 1.71 ± 0.57 mV (in dark) to 3.30 ± 0.81 mV (light on). Nevertheless, the increments in SP under illumination again indicate the p-type nature of P3HT and the creation of more holes by photoexcitation. In addition, the photo-induced charge separation may take place at the interfaces between samples and substrates,[43] leaving more holes in P3HT nanostructures. However, our results suggest that the photo-induced charge separation between P3HT and ITO substrates is not very efficient, as the increments upon photo-excitation is limited, only a couple to a few millivolts, as compared to the case of PPV on ITO substrates.[44]

Quantitative estimation of carrier density in P3HT nanostructures by EFM

EFM is a powerful scanning probe technique to measure electrostatic forces of charges on the sample, and have been shown capable of quantitatively survey the charge number in the nanostructures by varying the bias voltage V_{EFM} or the tip-sample distance z.[45] In EFM, the phase shift $\Delta\Phi$ caused by the electrostatic force at various V_{EFM} can be estimated by the following eqn (1)[46,47]

$$\Delta\Phi = A(V_{EFM} - V_S) + B(V_{EFM} - V_S)^2 \quad (1)$$

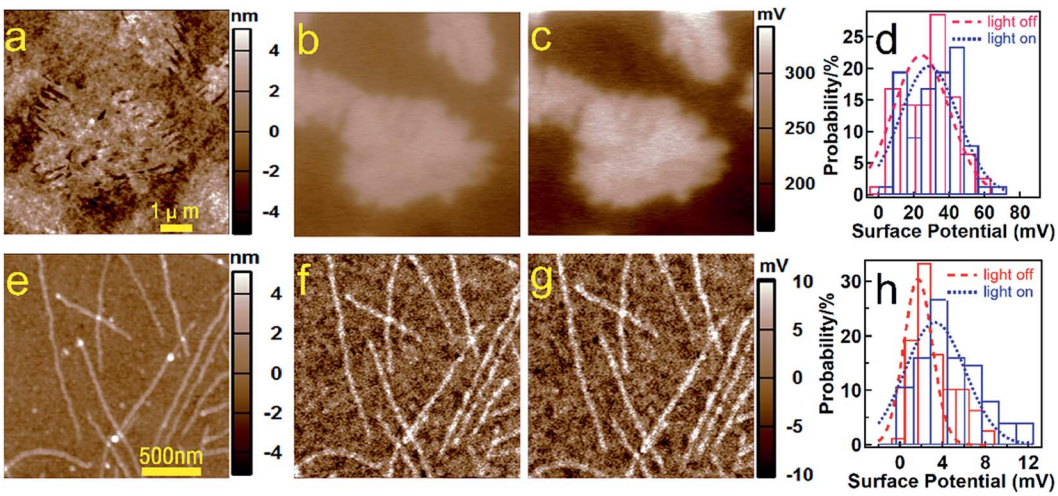

Fig. 2 Comparison between the P3HT islands and nanofibrils on the surface potential and the modulation by light. (a) Topography of P3HT islands; SKPM images of P3HT islands with light (b) off and (c) on; (d) the histograms of the surface potential of P3HT islands with light off (24.3 ± 7.1 mV) and on (28.8 ± 8.7 mV); (e) topography of P3HT nanofibrils; SKPM images of P3HT nanofibrils with light (f) off and (g) on; (h) the histograms of the surface potential of P3HT nanofibrils with light off (1.71 ± 0.57 mV) and on (3.30 ± 0.81 mV). The color bars of the images indicate the scale that colors represent.

$$A = \left(\frac{Q}{2k}\right)\left(\frac{Q_S h}{\varepsilon z^3}\right),\quad B = -\left(\frac{Q}{2k}\right)\left(\frac{3\varepsilon_0 Sh}{z^4}\right) \qquad (2)$$

where, the V_S is the surface potential from SKPM, $Q \sim 186$, $k \sim 8$ N m^{-1}, $\varepsilon \sim 4$, S is the effective area contributing to the electrostatic force, the average height of the islands h is ~3.5 nm, and the tip-substrate distance z is typically ~50 nm. In eqn (1), the first term denotes the contribution of the nano-structure charge Q_S, whereas the second term associated with the capacitive force between the tip and substrate. Fig. 3a–c show the images of phase shifts for P3HT nano-islands at a bias of −6 V, 0 V, and 6 V, respectively (see ESI Fig. S4† for all images at various bias voltages). It is a clear that the phase shift $\Delta\Phi$ (relative to the substrate) changes sign when the bias changes from −6 V to 6 V. Taking the same island area, the average $\Delta\Phi$ is measured as a function of V_{EFM}, as shown in Fig. 3d, where the blue circles and red boxes represent the phase shift of nano-islands in dark and under illumination, respectively. In both cases, the average $\Delta\Phi$ is negatively depended on the bias voltage. The polynomial fitting of the experimental data by eqn (1) gives the fitting parameters A and B, then A has been used to calculate the charges Q_S in the P3HT nano-islands and fibrils. The histogram of the estimated charge values in P3HT nano-islands is shown in the insert of Fig. 3d, and the red and blues bars refers to the dark and the light-on cases, respectively. It is clear that the distribution becomes broader at the high Q_S side once the excitation light is on, indicating more holes in P3HT islands, from $(2.9 \pm 1.1) \times 10^{-7}$ nC in dark to $(3.6 \pm 1.4) \times 10^{-7}$ nC under illumination, ~24% increment.

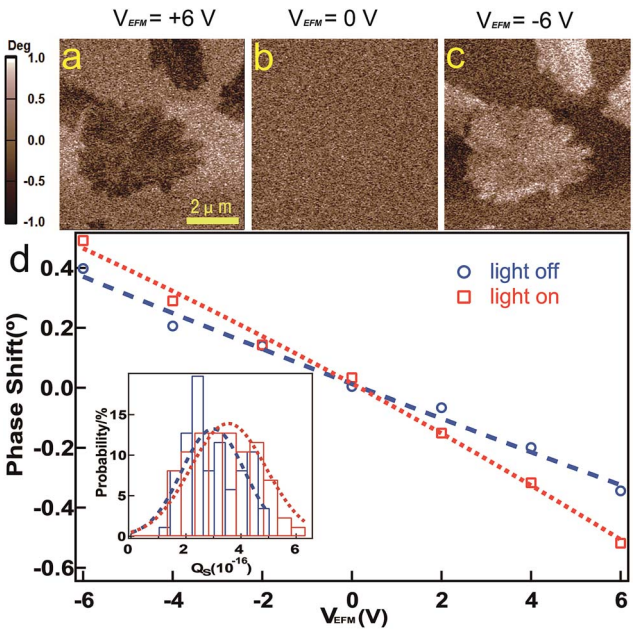

Fig. 3 EFM images of the P3HT islands with different bias and the estimation of the light-modulated charges. EFM images with a bias to the tip V_{EFM} of (a) +6 V, (b) 0 V, (c) −6 V, the insert is the histograms of the charge distribution light off ($Q_S = (2.9 \pm 1.1) \times 10^{-7}$ nC) and on ($Q_S = (3.6 \pm 1.4) \times 10^{-7}$ nC); (d) phase shift $\Delta\Phi$ *vs.* EFM bias V_{EFM} while light off (blue circles) and on (red boxes). The blue and red curves are the best polynomial fitting for $\Delta\Phi = A(V_{EFM} - V_S) + B(V_{EFM} - V_S)^2$, A and B are fitting parameters, V_s as a substrate potential.

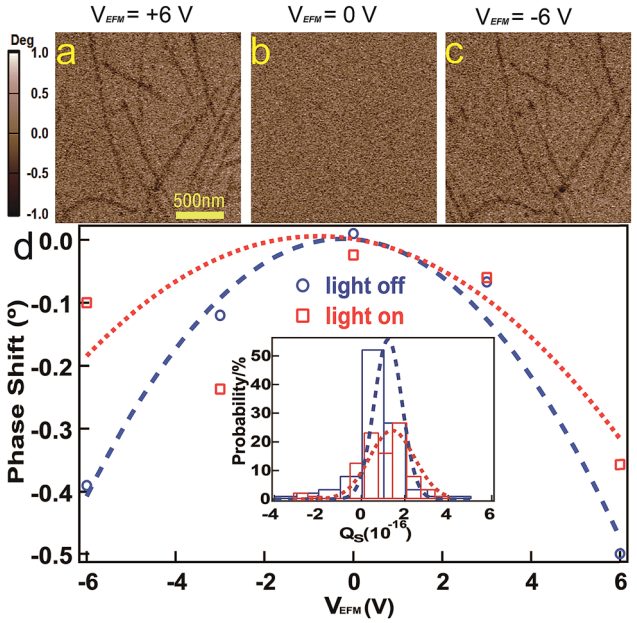

Fig. 4 EFM images of the P3HT nanofibrils with different bias and the estimation of the light-modulated charges. EFM images at V_{EFM} = (a) +6 V, (b) 0 V, and (c) −6 V; the insert is histograms of the charge distribution light off ($Q_S = (1.2 \pm 0.6) \times 10^{-7}$ nC) and on ($Q_S = (1.4 \pm 1.0) \times 10^{-7}$ nC); (d) phase shift $\Delta\Phi$ *vs.* EFM bias V_{EFM} while light off (blue circles) and light on (red boxes). The blue and red curves are the best fit for the polynomial law of $\Delta\Phi = A(V_{EFM} - V_S) + B(V_{EFM} - V_S)^2$, A and B are fitting parameters, V_s as a substrate potential.

The same measurements have also been carried out for P3HT nano-fibrils, and the results are shown in Fig. 4. Here, the phase shifts look more symmetric about the zero V_{EFM}, indicating a much smaller A in eqn (1). This is reasonable, because the diameter of fibrils (also the height, ~1.6 nm) is much smaller than the size (~10–20 nm) of the conducting tip, and thus the probing area of the tip covers most the ITO substrate, the EFM signal of which is symmetric as a conductor. Taking the height of nano-fibrils h of and the V_S from the SKPM results, polynomial fittings (Fig. 4d) are used again to estimate the charges in the fibrils. Similarly, the histograms (Fig. 4d insert) show the broadening of the distribution upon illumination, and the average charge increase ~15%, from $(1.2 \pm 0.6) \times 10^{-7}$ nC (dark) to $(1.4 \pm 1.0) \times 10^{-7}$ nC (light on). Both value are less than those obtained for nano-islands. This is consistent with the observation of more symmetric changes in phase shifts while varying the bias voltage in P3HT nano-fibrils. However, the quantitative estimation of charges depends on the effective area with charges probed by the EFM tip, which is about the size of the EFM tip in case of nano-islands but becomes smaller as the fibrils are "thinner". Therefore, the results from charge estimations imply that both nano-islands and fibrils show similar optoelectronic response upon excitation by light, and this is consistent with the similar π–π stacking

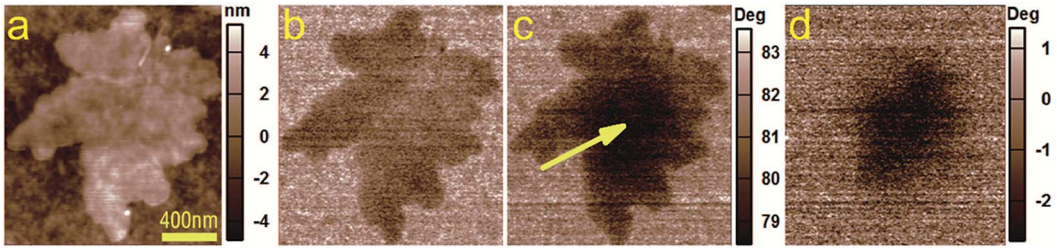

Fig. 5 The change of charges before and after injection in P3HT islands on Si/SiO_2. (a) Topography of an P3HT island; EFM images (phase shift, $V_{EFM} = 3$ V, $z = 50$ nm) of the same island (b) before charge injection and (c) after a local injection ($V_{INJ} = +5$ V for 200 s) on the central point (injection point marked by the arrow); (d) the differential EFM image, the changes in phase shift ($\Delta\Phi_{INJ} - \Delta\Phi_0$).

molecular architecture explored by AFM topographic imaging.

Holes injection into P3HT islands on silicon substrates

Heim *et al.* showed that ambipolar charges was injected into a single pentacene monolayer island, and higher ordered monolayer improved the delocalization of injected charges.[48] Here, better π–π stacking is expected for the nano-islands and fibrils as suggested by the AFM topography and EFM measurements on the charge density. To examine whether the π–π stacking in P3HT can also improve the charge distribution/transportation, charge injection experiments similar as reported[48] have been carried out on both nano-islands and fibrils of P3HT. In experiments, the conducting tip is in contact with the nanostructures with a DC voltage (V_{INJ}) between the tip and the substrate for a certain period. Then the topography of sample is imaged again to ensure no obvious morphology changes, and the EFM images are recorded to check any changes in the charges distribution in the nanostructures.

Unlike that both electrons and holes can be injected into the pentacene islands, we find that only holes can be injected into the nano-islands of P3HT on silicon wafers without changing the morphology of islands, as shown in Fig. 5. Before the charge injection, the island appears slightly dark in the EFM image ($V_{EFM} = +3$ V, Fig. 5b), and the relative phase shift with respect to the substrate $\Delta\Phi \approx -1.215°$. To inject charges into the islands, the tip is gently in contact with the islands at a typical force of ~600 pN and a V_{INJ} of +5 V for 200 seconds. After the injection, the EFM image is taken again under the same conductions (Fig. 5c), and a much darker region appears around the injection point as marked by the arrow, suggesting the success of holes injection. The relative phase shift with respect to the substrate $\Delta\Phi$ changes to $-3.253°$. Fig. 5d is the differential image between Fig. 5c and b, *i.e.* the EFM signal change after charge injection, showing the 2D distribution of injected holes with an average diameter of about 750 nm. The size of this distribution region of holes is much larger than that of the tip used in charge injection, demonstrating that those injected holes can delocalize in the nano-islands. This further suggest that the better π–π stacking improve the transportation of holes and in turn injection of more holes.

If charges are injected on the substrate at a position just outside the islands, there are no changes in EFM phase shift (ESI Fig. S5†). In addition, we also tried the injection of electrons by applying a negative voltage without success. Even at a small negative V_{INJ} of −1 V, the morphology of islands changes (ESI Fig. S6†). The injection of only holes in these P3HT nano-island is consistent with the p-type nature of P3HT. In contrast, the experiments of charge injection failed on P3HT nano-fibrils too (ESI Fig. S7†). This may be due to the very small diameter of the fibrils. In addition, the AFM topographic images show that the nano-fibrils is not uniform along the fibril axis, indicating the variations in the chain planarity, the crystallinity and the conjugation length of P3HT along the fibrils, which may act as defects to scatter charges while they are transported in such a one dimensional wire. This can lower the conductivity of the nano-fibrils, leading to the limited injection of both holes and electrons. The electrical conductivity have been reported for varied nanostructures and nanocomposites,[49–51] and for the composite of P3HT and dopants.[52] In this report, though the electrical conductivity was not directly measured, our results indicated the significantly different electrical conductivity between the nano-islands and fibrils is expected. These findings are essential for the fabrication of the P3HT-based nanocomposites and their applications.

4. Conclusion

Using different preparation protocols, P3HT can form various molecular architectures, *e.g.* nano-island and fibrils, besides normal spin-coating films. AFM topography of these nanostructures reveals a characteristic single-layer thickness of ~1.5–1.6 nm, which is the spacing between the side chains. This indicates a well π–π stacking of inter-molecular backbones, which is further confirmed by the Raman spectra. To characterize the optoelectronic properties of these nanostructures, SKPM and EFM are used. Positive changes in both the surface potential and charges in the nano-islands and fibrils have been observed. Quantitatively estimations of the photo-induced charges reveals an increments of holes is ~24% for nano-island and 15% for nano-fibrils of P3HT, respectively. This difference between these two nanostructures as measured by EFM may not be as significant as from the number, because the effective EFM probing area is different in these two cases. Nevertheless, the similar optoelectronic responses in nano-island and fibrils of P3HT imply the positive role of π–π stacking in improving the electronic property of P3HT

nanostructures. Further charge injection experiments show that holes can be injected into an island and delocalized among the island. This demonstrate the excellent hole propagation behavior in the nano-island structures, which is useful for organic molecule-based, more specifically P3HT-based, devices. Therefore, SKPM and EFM technique could provide an effective way to gain direct information on the surface potential and charges generation/separation of nanostructures by combining with laser irradiation. This method would be important for both basic understanding and potential applications of nanostructures in optoelectronics and photovoltaics.

Acknowledgements

We gratefully acknowledge support from the Research Start Fund for Talent Recruitment, Chongqing University, and the fundamental and advanced research program of Chongqing (grant # cstc2013jcyjA10047), China.

References

1 A. Facchetti, *Chem. Mater.*, 2011, **23**, 733–758.
2 P. M. Beaujuge and J. M. Frechet, *J. Am. Chem. Soc.*, 2011, **133**, 20009–20029.
3 O. J. Dautel, M. Robitzer, J. C. Flores, D. Tondelier, F. Serein-Spirau, J. P. Lere-Porte, D. Guerin, S. Lenfant, M. Tillard, D. Vuillaume and J. J. Moreau, *Chemistry*, 2008, **14**, 4201–4213.
4 K. Nataliya, J. Evelin, A. Hans-Juergen, S. Mareike, K. Anton, G. Ganna, M. Sergiy, J. Dieter, S. Paul, A. F. Andrey and S. Manfred, *Nano Lett.*, 2003, **3**, 707–712.
5 M. T. Dang, L. Hirsch and G. Wantz, *Adv. Mater.*, 2011, **23**, 3597–3602.
6 H. Sirringhaus, P. J. Brown, R. H. Friend, M. M. Nielsen, K. Bechgaard, B. M. W. Langeveld-Voss, A. J. H. Spiering, R. A. J. Janssen, E. W. Meijer, P. Herwig and D. M. de Leeuw, *Nature*, 1999, **401**, 685–688.
7 M. Brinkmann and J. C. Wittmann, *Adv. Mater.*, 2006, **18**, 860–863.
8 M. Brinkmann, *J. Polym. Sci., Part B: Polym. Phys.*, 2011, **49**, 1218–1233.
9 T. Yamamoto, *NPG Asia Mater.*, 2010, **2**, 54–60.
10 T. J. Prosa and M. J. Winokur, *Macromolecules*, 1992, **25**, 4364–4372.
11 R. D. McCullough, S. Tristram-Nagle, S. P. Williams, R. D. Lowevt and M. Jayaramant, *J. Am. Chem. Soc.*, 1993, **115**, 4910–4911.
12 J. Liu, M. Arif, J. Zou, S. I. Khondaker and L. Zhai, *Macromolecules*, 2009, **42**, 9390–9393.
13 S. Samitsu, T. Shimomura, S. Heike, T. Hashizume and K. Ito, *Macromolecules*, 2008, **41**, 8000–8010.
14 C. M. Rodd and R. Agarwal, *Nano Lett.*, 2011, **11**, 3460–3467.
15 C. M. Rodd and R. Agarwal, *Nano Lett.*, 2013, **13**, 3760–3765.
16 E. J. Crossland, K. Tremel, F. Fischer, K. Rahimi, G. Reiter, U. Steiner and S. Ludwigs, *Adv. Mater.*, 2012, **24**, 839–844.
17 M. Brinkmann, *J. Polym. Sci., Part B: Polym. Phys.*, 2011, **49**, 1218–1233.
18 E. T. Niles, J. D. Roehling, H. Yamagata, A. J. Wise, F. C. Spano, A. J. Moulé and J. K. Grey, *J. Phys. Chem. Lett.*, 2012, **3**, 259–263.
19 K. W. Chou, B. Yan, R. Li, E. Q. Li, K. Zhao, D. H. Anjum, S. Alvarez, R. Gassaway, A. Biocca, S. T. Thoroddsen, A. Hexemer and A. Amassian, *Adv. Mater.*, 2013, **25**, 1923–1929.
20 H. Yang, S. W. LeFevre, C. Y. Ryu and Z. Bao, *Appl. Phys. Lett.*, 2007, **90**, 172116.
21 Y. Yuan, J. Shu, P. Liu, Y. Zhang, Y. Duan and J. Zhang, *J. Phys. Chem. B*, 2015, **119**, 8446–8456.
22 F. C. Spano and C. Silva, *Annu. Rev. Phys. Chem.*, 2014, **65**, 477–500.
23 H. Yamagata and F. C. Spano, *J. Chem. Phys.*, 2012, **136**, 184901.
24 F. C. Spano, *J. Am. Chem. Soc.*, 2009, **131**, 4267–4278.
25 J.-C. Bolsée, W. D. Oosterbaan, L. Lutsen, D. Vanderzande and J. Manca, *Adv. Funct. Mater.*, 2013, **23**, 862–869.
26 S. Berson, R. de Bettignies, S. Bailly and S. Guillerez, *Adv. Funct. Mater.*, 2007, **17**, 1377–1384.
27 G. A. O'Brien, A. J. Quinn, D. A. Tanner and G. Redmond, *Adv. Mater.*, 2006, **18**, 2379–2383.
28 M. Arif, J. Liu, L. Zhai and S. I. Khondaker, *Appl. Phys. Lett.*, 2010, **96**, 243304.
29 S. Ren, L. Y. Chang, S. K. Lim, J. Zhao, M. Smith, N. Zhao, V. Bulovic, M. Bawendi and S. Gradecak, *Nano Lett.*, 2011, **11**, 3998–4002.
30 H. Wei, X. Yan, Y. Li, S. Wu, A. Wang, S. Wei and Z. Guo, *J. Phys. Chem. C*, 2012, **116**, 4500–4510.
31 J. Zhu, S. Wei, M. Alexander Jr, T. D. Dang, T. C. Ho and Z. Guo, *Adv. Funct. Mater.*, 2010, **20**, 3076–3084.
32 H. Gu, X. Zhang, H. Wei, Y. Huang, S. Wei and Z. Guo, *Chem. Soc. Rev.*, 2013, **42**, 5907–5943.
33 J. Zhu, H. Gu, J. Guo, M. Chen, H. Wei, Z. Luo, H. A. Colorado, N. Yerra, D. Ding, T. C. Ho, N. Haldolaarachchige, J. Hopper, D. P. Young, Z. Guo and S. Wei, *J. Mater. Chem. A*, 2014, **2**, 2256–2265.
34 J. Gao, J. D. Roehling, Y. Li, H. Guo, A. J. Moulé and J. K. Grey, *J. Mater. Chem. C*, 2013, **1**, 5638.
35 S. Wood, O. Garnett, N. Tokmoldin, W. C. Tsoi, S. A. Haque and J. S. Kim, *R. Soc. Chem., Spec. Publ.*, 2014, **174**, 267–279.
36 S. Sun, T. Salim, L. H. Wong, Y. L. Foo, F. Boey and Y. M. Lam, *J. Mater. Chem.*, 2011, **21**, 377–386.
37 R. D. McCullough, S. Tristram-Nagle, S. P. Williams, R. D. Lowevt and M. Jayaramant, *J. Am. Chem. Soc.*, 1993, **115**, 4910–4911.
38 J. Mårdalen, E. J. Samuelsen and A. Pedersen, *Synth. Met.*, 1993, **55**, 378–383.
39 W. C. Tsoi, D. T. James, J. S. Kim, P. G. Nicholson, C. E. Murphy, D. D. Bradley and J. Nelson, *J. Am. Chem. Soc.*, 2011, **133**, 9834–9843.
40 M. Baghgar, E. Pentzer, A. J. Wise, J. A. Labastide, T. Emrick and M. D. Barnes, *ACS Nano*, 2013, **7**, 8917–8923.
41 M. Baghgar, A. M. Barnes, E. Pentzer, A. J. Wise, B. A. Hammer, T. Emrick, A. D. Dinsmore and M. D. Barnes, *ACS Nano*, 2014, **8**, 8344–8349.

42 A. Liscio, G. D. Luca, F. Nolde, V. Palermo, K. MÜllen and P. Samorì, *J. Am. Chem. Soc.*, 2008, **130**, 780–781.
43 A. Liscio, V. Palermo and P. Samori, *Acc. Chem. Res.*, 2010, **43**, 541–550.
44 R. Liu, *J. Phys. Chem. C*, 2009, **113**, 9368–9374.
45 S. E. Yalcin, J. A. Labastide, D. L. Sowle and M. D. Barnes, *Nano Lett.*, 2011, **11**, 4425–4430.
46 S. Wu, Z. L. Wu, D. D. Lin, Z. Y. Zhong, Z. M. Jiang and X. J. Yang, *Nanoscale Res. Lett.*, 2014, **9**, 245.
47 T. Mélin, H. Diesinger, D. Deresmes and D. Stiévenard, *Phys. Rev. B: Condens. Matter Mater. Phys.*, 2004, **69**, 035321.
48 T. Heim, K. Lmimouni and D. Vuillaume, *Nano Lett.*, 2004, **4**, 2145–2150.
49 X. Zhang, J. Zhu, N. Haldolaarachchige, J. Ryu, D. P. Young, S. Wei and Z. Guo, *Polymer*, 2012, **53**, 2109–2120.
50 X. Zhang, Q. He, H. Gu, H. A. Colorado, S. Wei and Z. Guo, *ACS Appl. Mater. Interfaces*, 2013, **5**, 898–910.
51 X. Zhang, X. Yan, J. Guo, Z. Liu, D. Jiang, Q. He, H. Wei, H. Gu, H. A. Colorado, X. Zhang, S. Wei and A. Z. Guo, *J. Mater. Chem. C*, 2015, **3**, 162–176.
52 D. T. Scholes, S. A. Hawks, P. Y. Yee, H. Wu, J. R. Lindemuth, S. H. Tolbert and B. J. Schwartz, *J. Phys. Chem. Lett.*, 2015, **6**, 4786–4793.